



Optically-detected NMR of defect sites in  $\text{EuVO}_4$   
by Yongchen Sun

A thesis submitted in partial fulfillment of the requirements for the degree of Doctor of Philosophy in Physics

Montana State University

© Copyright by Yongchen Sun (1993)

Abstract:

This thesis reports laser spectroscopic studies of stoichiometric  $\text{EuVO}_4$  and isomorphous compounds. Electronic and hyperfine structures have been used to study the electron-phonon coupling and the nature of the lattice defects.

Conventional absorption, fluorescence, and Raman scattering spectroscopy was used to study the  $\text{Eu}^{3+}$  energy levels of  $\text{EuVO}_4$ ,  $\text{EuAsO}_4$ ,  $\text{Eu}^{3+}:\text{YVO}_4$ ,  $\text{Eu}^{3+}:\text{LuVO}_4$ ,  $\text{Eu}^{3+}:\text{YPO}_4$ , and  $\text{Eu}^{3+}:\text{TuPO}_4$ . Crystal field calculations were also carried out for these compounds. The  $\text{Eu}^{3+} 7F_1$  singlet levels in  $\text{EuVO}_4$  and  $\text{EuAsO}_4$  were found to exhibit Davydov splittings, a result of the ion-ion interaction in the stoichiometric compounds. The  $\text{Eu}^{3+} 7F_j$  2 doublet levels all have anomalously small Lande g factor for the vanadates and  $\text{EuAsO}_4$ , a result of the dynamic Jahn-Teller effect due to electron-phonon coupling.

$\text{EuVO}_4$  had been found previously to have over 50 satellite lines in the  $7F_0 - 5D_0$  region, each line corresponding to a distinct defect site. Defect line maps were measured for two additional growths of  $\text{EuVO}_4$ . Time-resolved fluorescence has been used to study the pathways of the energy migration among these sites. For example, the site at 515868 GHz was found to transfer its energy to other sites in 50 fs. Systematics of the rare earth spectra were considered, and a simple relationship between the energy levels and the lattice cell size of the host material has been suggested.

Spectral holeburning and optically-detected nuclear-magnetic-resonance (ODNMR) measurements have been used to study the hyperfine structure of the defect sites; each was found to possess a distinct hyperfine interaction. Ground state quadrupole interaction parameters (P, T) are given for over 30 defect sites. A new holeburning mechanism -energy-transfer enhanced holeburning was proposed. The full angle-dependent ODNMR study of some of the defect sites yielded information about the ground state nuclear magnetic shielding parameters and the principal axes of the ground state quadrupole interaction. The site with  $7F_q - 3D_0$  transition at 515868 GHz was found to have a quadrupole coordinate system tilted  $10.7^\circ$  and a very anisotropic nuclear magnetic moment, only 5% of the bare nucleus value in the defect x direction. This is the first time this kind of information is obtained for a defect site with no predetermined structural information. It should provide the basis for further theoretical calculations and the final determination of the lattice defect local structure.

OPTICALLY-DETECTED NMR OF DEFECT SITES IN  $\text{EuVO}_4$

by

Yongchen Sun

A thesis submitted in partial fulfillment  
of the requirements for the degree

of

Doctor of Philosophy

in

Physics

MONTANA STATE UNIVERSITY  
Bozeman, Montana

November 1993

D378  
Sw71

APPROVAL  
of a thesis submitted by

Yongchen Sun

This thesis has been read by each member of the thesis committee and has been found to be satisfactory regarding content, English usage, format, citations, bibliographic style, and consistency, and is ready for submission to the College of Graduate Studies.

11 November 1993  
Date

Rufus L. Cone  
Chairman, Graduate Committee

Approved for the Major Department

11-11-93  
Date

[Signature]  
Head, Major Department

Approved for the College of Graduate Studies

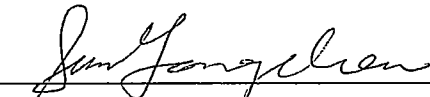
11/14/93  
Date

[Signature]  
Graduate Dean

## STATEMENT OF PERMISSION TO USE

In presenting this thesis in partial fulfillment of the requirements for a doctoral degree at Montana State University, I agree that the Library shall make it available to borrowers under rules of the Library. I further agree that copying of this thesis is allowable only for scholarly purposes, consistent with "fair use" as prescribed in the U.S. Copyright Law. Requests for extensive copying or reproduction of this thesis should be referred to University Microfilms International, 300 North Zeeb Road, Ann Arbor, Michigan 48106, to whom I have granted "the exclusive right to reproduce and distribute copies of the dissertation for sale in and from microform or electronic format, along with the right to reproduce and distribute my abstract in any format in whole or in part."

Signature



Date

11 November 93

## ACKNOWLEDGEMENTS

The author wishes to thank a number of people, without whom the completion of this thesis would have been impossible. First and foremost, he wants to thank his advisor, Professor Rufus L. Cone, for his scientific guidance, inexhaustible ideas, patience, and encouragement. Thanks are also extended to Dr. M.J.M. Leask, with whom the author had wonderful collaboration in the laboratory, and to Dr. M.M. Abraham, who provided encouragement and many of the crystals studied in this thesis.

The author also wishes to acknowledge the technical assistance of Norman Williams and Erik Andersen, and the help he received from his fellow students: Raymond P. Jones, Randy W. Equall, Margaret Hall, and Guangming Wang. Last but not least, he wants to thank his wife and parents for their love and support over the years.

## TABLE OF CONTENTS

	Page
APPROVAL .....	ii
STATEMENT OF PERMISSION TO USE.....	iii
ACKNOWLEDGEMENTS .....	iv
TABLE OF CONTENTS .....	v
LIST OF TABLES .....	viii
LIST OF FIGURES .....	x
ABSTRACT .....	xiv
1. INTRODUCTION.....	1
2. PRIMARY SPECTROSCOPY AND CRYSTAL FIELD ANALYSES.....	9
Experiments .....	10
Absorption Experiments .....	10
Fluorescence Experiments.....	12
Laser Excitation.....	13
Sample Temperature.....	13
Cryostat and Magnetic Fields.....	13
Selection Rules.....	14
Crystals .....	15
General Results .....	17
$^5D_J$ Levels .....	17
$^7F_J$ Levels.....	20
Results for Concentrated Crystals.....	22
$^7F_0 - ^5D_0$ Defect Spectra for $\text{EuVO}_4$ .....	22
Fluorescence.....	30
$^7F_J - ^5D_J$ Transitions.....	34

TABLE OF CONTENTS---Continued

	Page
Zeeman Experiments .....	38
${}^7F_0$ - ${}^5D_J$ Transitions .....	38
${}^5D_0$ - ${}^7F_J$ Transitions .....	42
Crystal Field Analysis .....	45
 3. JAHN-TELLER EFFECT AND ION-ION INTERACTION .....	 48
Introduction .....	48
Raman Scattering Selection Rules .....	50
Raman Scattering Experiments .....	52
Phonon Scattering .....	52
Electronic Raman Scattering .....	57
Zeeman Experiments .....	61
Jahn-Teller Effects .....	68
Jahn-Teller Theorem .....	68
Ham Quenching .....	69
Ham Quenching in Europium Compounds .....	73
Ion-ion Interactions and Davydov splitting .....	74
 4. DEFECT STRUCTURE AND DYNAMICS .....	 77
Systematics of Rare Earth Ion Spectra .....	78
Ions in Hosts with Different Anions .....	80
Ions in Hosts with the Same Anions .....	81
Concentration Effect of the Active Ion .....	83
Temperature Effect .....	86
Defect Site Fluorescence .....	86
Defect Site Fluorescence without Time Resolution .....	86
Time-resolved Fluorescence .....	88
Discussion .....	93
 5. SPECTRAL HOLEBURNING AND ODNMR .....	 96
The Nuclear Quadruple Hamiltonian .....	97
General Treatment .....	97
Quadrupole Interaction .....	99
Nuclear Magnetic Shielding .....	101
The Holeburning Process .....	102
Basic Mechanism .....	102

TABLE OF CONTENTS---Continued

	Page
Axial Sites .....	105
Non-axial Sites .....	105
Optically-Detected Nuclear-Magnetic-Resonance .....	106
Experimental Setup .....	107
Zero Field ODNMR Results .....	111
Discussions .....	121
Energy-Transfer Enhanced Holeburning .....	121
Quadrupole Moment Ratio .....	123
Asymmetry Parameters .....	125
Electronic vs. Lattice Contributions in the Ground State .....	127
Correlation of P and B <sub>20</sub> .....	129
6. ANGLE-DEPENDENT ODNMR OF DEFECT SITES IN EuVO <sub>4</sub> .....	131
ODNMR of a Defect System in a D <sub>4h</sub> Crystal .....	133
Symmetry Consequences .....	133
Matrix Solving Algorithm .....	135
Fitting of Experimental Data .....	137
Experimental Setup .....	140
Angle-Dependent ODNMR Results .....	142
Line D .....	145
Line A .....	152
Line #39 .....	156
Line E .....	160
Lines F and G .....	160
Line O .....	161
Possibility of ODNMR on the Intrinsic Site .....	164
Conclusions .....	165
APPENDICES .....	166
I Conversion of the Wavemeter Readings .....	167
II Observed and Calculated Energy Levels .....	170
III Coordinate Transformation Using Euler Angles .....	178
IV Fitting Programs .....	181
REFERENCES CITED .....	197



## LIST OF TABLES

	Page
Table 2.1 Selection rules in $D_{2d}$ symmetry .....	15
Table 2.2 Crystals studied .....	17
Table 2.3 Splittings at a field of 55 kG along the $c$ direction .....	42
Table 2.4 Fitted crystal field parameters in vanadates and phosphates .....	46
Table 3.1 Allowed scattering symmetries and their related second-order susceptibilities for groups $D_{4h}$ and $D_{2d}$ .....	50
Table 3.2 Scattering geometry and allowed excitations .....	52
Table 3.3 Phonon frequencies ( $\text{cm}^{-1}$ ) of the vanadates measured at 77 K .....	54
Table 3.4 Energy levels in $\text{EuVO}_4$ and $\text{EuAsO}_4$ as determined by Raman scattering .....	61
Table 3.5 ${}^7\text{F}_1$ levels measured by different method in the stoichiometric europium compounds .....	74
Table 4.1 $\text{Eu}^{3+} {}^7\text{F}_0 - {}^5\text{D}_0$ energy in different hosts .....	80
Table 4.2 Energy levels of $\text{Eu}^{3+}$ doped $\text{YVO}_4$ and $\text{LuPO}_4$ .....	83
Table 5.1 ${}^7\text{F}_0$ ODNMR peaks and quadrupole parameters for defect sites of the growth A crystal of $\text{EuVO}_4$ .....	112
Table 5.2 ${}^7\text{F}_0$ ODNMR peaks and quadrupole parameters for defect sites in the ORNL crystal of $\text{EuVO}_4$ .....	113

LIST OF TABLES---Continued

	Page
Table 5.3 Comparison of the ${}^7F_0$ ODNMR results of the high energy lines in the growth I crystal .....	120
Table 5.4 Europium quadrupole moment ratios .....	124
Table 5.5 Nuclear quadrupole asymmetry parameters for ${}^7F_0$ and ${}^5D_0$ states of $\text{EuVO}_4$ .....	127
Table 5.6 Comparison of quadrupole splittings and crystal field .....	130

## LIST OF FIGURES

	Page
Figure 1.1 Schematic representation of the tetragonal zircon structure ( $D_{4h}^{19}$ ) for $\text{RMO}_4$ . (R $\equiv$ rare earth, M $\equiv$ V, As, or P) .....	2
Figure 1.2 Simplified energy level diagram of an $\text{Eu}^{3+}$ ion.....	4
Figure 2.1 Experimental setup.....	11
Figure 2.2 The ${}^5\text{D}_0 - {}^7\text{F}_2 (\Gamma_4)$ spectrum for europium-doped vanadates and $\text{EuAsO}_4$ at 1.5 K.....	23
Figure 2.3 Comparison of the fluorescence and absorption spectra of the $\text{EuVO}_4 {}^7\text{F}_2 (\Gamma_4) \leftrightarrow {}^5\text{D}_0$ transition.....	24
Figure 2.4 The ${}^7\text{F}_0 - {}^5\text{D}_0$ defect spectrum of the ORNL $\text{EuVO}_4$ crystal .....	26
Figure 2.5 Expanded view of Figure 2.4 in the intrinsic site transition region for $\text{EuVO}_4$ .....	27
Figure 2.6. The ${}^7\text{F}_0 - {}^5\text{D}_0$ defect spectrum of the $\text{Pr}^{3+}$ doped $\text{EuVO}_4$ crystal .....	28
Figure 2.7 Expanded view of Figure 2.6 in the intrinsic transition region for $\text{EuVO}_4$ .....	29
Figure 2.8 The ${}^7\text{F}_1$ energy levels of $\text{EuVO}_4$ as measured by ${}^5\text{D}_0 - {}^7\text{F}_1$ fluorescence in a field of 40.0 kG.....	32
Figure 2.9 The ${}^5\text{D}_0 - {}^7\text{F}_1$ spectrum of $\text{EuAsO}_4$ in a field of 59.0 kG .....	33
Figure 2.10 Polarized $\text{EuVO}_4 {}^7\text{F}_1 - {}^5\text{D}_0$ absorption spectra at $T \approx 100$ K.....	35
Figure 2.11 Polarized $\text{EuVO}_4 {}^7\text{F}_1 - {}^5\text{D}_1$ absorption spectra at $T \approx 100$ K.....	36
Figure 2.12 Polarized $\text{EuAsO}_4 {}^7\text{F}_1 - {}^5\text{D}_1$ absorption spectra at $T \approx 100$ K. ....	37

## LIST OF FIGURES---Continued

	Page
Figure 2.13 The $^5D_3$ spectra of $\text{EuVO}_4$ in a field parallel to the $c$ -axis.....	40
Figure 2.14 The $^5D_3$ spectra of $\text{EuVO}_4$ in a field perpendicular to the $c$ -axis.....	41
Figure 2.15 Zeeman spectra of the $^5D_0 - ^7F_1$ transition in $\text{EuAsO}_4$ .....	43
Figure 3.1 Raman scattering of a tetragonal crystal .....	52
Figure 3.2 Raman scattering spectrum of $\text{EuAsO}_4$ at $T=1.5$ K.....	55
Figure 3.3 Raman scattering spectrum of $\text{EuVO}_4$ in the lower phonon frequency region .....	56
Figure 3.4 Comparison of the $\text{EuVO}_4$ and $0.1\% \text{Eu}^{3+}:\text{YVO}_4$ $\Gamma_1^+$ phonon scattering spectra .....	58
Figure 3.5 Electronic Raman Scattering spectrum for $\text{EuVO}_4$ $^7F_1$ levels .....	59
Figure 3.6 Electronic Raman scattering spectrum for $\text{EuAsO}_4$ $^7F_1$ levels.....	60
Figure 3.7 Raman scattering spectrum of $\text{EuVO}_4$ $^7F_1$ ( $\Gamma_5$ ) in a field of 50.0 kG along the $c$ -axis.....	64
Figure 3.8 Raman scattering spectrum of $\text{EuVO}_4$ $^7F_2$ ( $\Gamma_5$ ) in a field of 50.0 kG along the $c$ -axis.....	65
Figure 3.9 Raman scattering spectrum of $\text{EuAsO}_4$ $^7F_1$ ( $\Gamma_5$ ) in a field of 50.0 kG along the $c$ -axis.....	66
Figure 3.10 Raman scattering spectrum of $\text{EuAsO}_4$ $^7F_2$ ( $\Gamma_5$ ) in a field of 50.0 kG along the $c$ -axis .....	67
Figure 4.1 The variation of the $\text{Eu}^{3+}$ $^5D_1$ levels with the europium concentration in $\text{Eu}:\text{YPO}_4$ .....	84
Figure 4.2 The variation of the $\text{Eu}^{3+}$ $^5D_2$ levels with the europium concentration in $\text{Eu}:\text{YPO}_4$ .....	85

## LIST OF FIGURES---Continued

	Page
Figure 4.3 The ${}^5D_0 - {}^7F_1$ fluorescence spectra when different ${}^5D_0$ defect lines were excited .....	89
Figure 4.4 Time resolved ${}^5D_0 - {}^7F_1$ fluorescence spectra when pumping the 515868 GHz defect line in $\text{EuVO}_4$ .....	91
Figure 4.5 The ${}^5D_0 - {}^7F_1$ fluorescence spectra of the site at 515979 GHz in $\text{EuVO}_4$ .....	92
Figure 5.1 The holeburning process for an $I=5/2$ system with singlet electronic states.....	103
Figure 5.2 Zero field ODNMR spectrum for line Q of the growth A $\text{EuVO}_4$ crystal, showing large signals due to ground state resonances and smaller signals of opposite polarity due to excited state resonances .....	108
Figure 5.3 Block diagram of the ODNMR experimental setup.....	110
Figure 5.4 Inhomogeneous lineshape of the ${}^{151}\text{Eu}$ "1/2 to 3/2" nuclear hyperfine transition for line D in the growth A $\text{EuVO}_4$ crystal.....	115
Figure 5.5 Excitation profile of the ${}^7F_0 - {}^5D_0$ intrinsic transition for 0.5% $\text{Eu}^{3+}:\text{YPO}_4$ , in a magnetic field of 55 kG, showing long-lived holes in the intrinsic transition.....	117
Figure 6.1 Stereographic projections of the $D_{2d}$ and $D_{4h}$ groups.....	134
Figure 6.2 The splitting scheme of the nuclear hyperfine levels .....	138
Figure 6.3 Diagram of the rotating gear system showing both the top view and the side view .....	141
Figure 6.4 The ODNMR spectrum of the ${}^{151}\text{Eu}$ "1/2 to 3/2" transition for line D in $\text{EuVO}_4$ .....	143
Figure 6.5 The ODNMR spectrum of the ${}^{151}\text{Eu}$ "1/2 to 3/2" transition for line D with a magnetic field of 2 kG along the c axis in $\text{EuVO}_4$ .....	144

## LIST OF FIGURES---Continued

	Page
Figure 6.6 The ODNMR spectrum of the $^{151}\text{Eu}$ "1/2 to 3/2" transition for line D with a magnetic field of 2 kG at 31 degrees from the $c$ -axis in the $c$ - $a$ plane in $\text{EuVO}_4$ .....	146
Figure 6.7 The ODNMR spectrum of the $^{151}\text{Eu}$ "1/2 to 3/2" transition for line D with a magnetic field of 2 kG at 60 degrees from the $c$ -axis in the $c$ - $a$ plane in $\text{EuVO}_4$ .....	147
Figure 6.8 The ODNMR spectrum of the $^{151}\text{Eu}$ "1/2 to 3/2" transition for line D with a magnetic field of 2 kG along the $a$ -axis in $\text{EuVO}_4$ .....	148
Figure 6.9 Constant field ( $H = 2.00$ kG) angle-dependent ODNMR spectra of line D (515979 GHz) in $\text{EuVO}_4$ .....	150
Figure 6.10 The ODNMR spectra with magnetic field in the $a$ - $a'$ plane for the same $\text{EuVO}_4$ transition as Figure 6.9.....	151
Figure 6.11 Constant field ( $H = 5.00$ kG) ODNMR spectra as a function of the angle between the field and the $c$ -axis in the $c$ - $a$ plane. The data are for the $^{151}\text{Eu}$ "1/2 - 3/2" transition for the defect line at 515868 GHz or $17207.50\text{ cm}^{-1}$ in $\text{EuVO}_4$ .....	154
Figure 6.12 Constant field ( $H = 5.00$ kG) ODNMR spectrum for the same $\text{EuVO}_4$ transition as that shown in Fig. 6.11, but with the field direction being rotated in the $a$ - $a'$ plane.....	155
Figure 6.13 Constant field ( $H = 3.00$ kG) angle-dependent ODNMR spectrum for line #39 of the growth I $\text{EuVO}_4$ Crystal. The field is in the $c$ - $a$ plane. Only the $^{151}\text{Eu}$ "1/2 - 3/2" transitions are shown.....	158
Figure 6.14 Constant field ( $H = 3.00$ kG) angle-dependent ODNMR spectrum for line #39 of the growth I $\text{EuVO}_4$ Crystal. The field is in the $c$ - $a$ plane. Only the $^{151}\text{Eu}$ "3/2 - 5/2" transitions are shown.....	159
Figure 6.15 Zeeman effect of the ODNMR spectra of lines F and G with the magnetic field along the $c$ -axis in $\text{EuVO}_4$ .....	162
Figure 6.16 Zeeman effect of the ODNMR spectra of lines F and G with the magnetic field along the $a$ -axis in $\text{EuVO}_4$ .....	163

## ABSTRACT

This thesis reports laser spectroscopic studies of stoichiometric  $\text{EuVO}_4$  and isomorphous compounds. Electronic and hyperfine structures have been used to study the electron-phonon coupling and the nature of the lattice defects.

Conventional absorption, fluorescence, and Raman scattering spectroscopy was used to study the  $\text{Eu}^{3+}$  energy levels of  $\text{EuVO}_4$ ,  $\text{EuAsO}_4$ ,  $\text{Eu}^{3+}:\text{YVO}_4$ ,  $\text{Eu}^{3+}:\text{LuVO}_4$ ,  $\text{Eu}^{3+}:\text{YPO}_4$ , and  $\text{Eu}^{3+}:\text{LuPO}_4$ . Crystal field calculations were also carried out for these compounds. The  $\text{Eu}^{3+}$   ${}^7\text{F}_1$  singlet levels in  $\text{EuVO}_4$  and  $\text{EuAsO}_4$  were found to exhibit Davydov splittings, a result of the ion-ion interaction in the stoichiometric compounds. The  $\text{Eu}^{3+}$   ${}^7\text{F}_{1,2}$  doublet levels all have anomalously small Landé  $g$  factor for the vanadates and  $\text{EuAsO}_4$ , a result of the dynamic Jahn-Teller effect due to electron-phonon coupling.

$\text{EuVO}_4$  had been found previously to have over 50 satellite lines in the  ${}^7\text{F}_0 - {}^5\text{D}_0$  region, each line corresponding to a distinct defect site. Defect line maps were measured for two additional growths of  $\text{EuVO}_4$ . Time-resolved fluorescence has been used to study the pathways of the energy migration among these sites. For example, the site at 515868 GHz was found to transfer its energy to other sites in 50  $\mu\text{s}$ . Systematics of the rare earth spectra were considered, and a simple relationship between the energy levels and the lattice cell size of the host material has been suggested.

Spectral holeburning and optically-detected nuclear-magnetic-resonance (ODNMR) measurements have been used to study the hyperfine structure of the defect sites; each was found to possess a distinct hyperfine interaction. Ground state quadrupole interaction parameters ( $P$ ,  $\eta$ ) are given for over 30 defect sites. A new holeburning mechanism - energy-transfer enhanced holeburning was proposed. The full angle-dependent ODNMR study of some of the defect sites yielded information about the ground state nuclear magnetic shielding parameters and the principal axes of the ground state quadrupole interaction. The site with  ${}^7\text{F}_0 - {}^5\text{D}_0$  transition at 515868 GHz was found to have a quadrupole coordinate system tilted  $10.7^\circ$  and a very anisotropic nuclear magnetic moment, only 5% of the bare nucleus value in the defect  $x$  direction. This is the first time this kind of information is obtained for a defect site with no predetermined structural information. It should provide the basis for further theoretical calculations and the final determination of the lattice defect local structure.

## CHAPTER 1

## INTRODUCTION

The rare earth vanadate family crystallize in the tetragonal zircon structure ( $D_{4h}^{19}$ ), with the exception of  $\text{LaVO}_4$  which crystallizes in the monoclinic monazite structure. The rare earth phosphates crystallize both in the zircon and in the monazite structures, with the heavier and smaller ions ( $\text{Gd}^{3+}$  to  $\text{Lu}^{3+}$ , including  $\text{Y}^{3+}$ ) going to the former and lighter and larger ions ( $\text{La}^{3+}$  to  $\text{Eu}^{3+}$ ) going to the latter.  $\text{EuAsO}_4$  also has tetragonal zircon structure. A schematic representation of the tetragonal zircon structure is shown in Figure 1.1. The crystal  $c$ -axis is shown as the  $z$  axis. The  $a$  and  $a'$  axes, parallel to the natural crystal surfaces, are shown as  $x$  and  $y$ . The rare earth ions occupy sites with  $D_{2d}$  local symmetry. The two-fold axes of  $D_{2d}$  are parallel to  $(x', y', z')$ , where  $(x', y')$  are in the basal plane and at  $45^\circ$  to  $(a, a')$ , respectively.

The tetragonal zircon crystals have a high pressure phase at  $P \sim 1$  GPa where they undergo a phase transition to the scheelite structure ( $C_{4h}$ ), resulting in a more efficient packing of the coordination polyhedra (Jayaraman *et al.* 1987, Chen *et al.* 1992). The high pressure phase transition of  $\text{Eu}^{3+}:\text{YVO}_4$  was studied using Raman scattering, and it was found that the scheelite structure was almost stable. When relieving the pressure to the atmosphere, the Raman scattering spectrum would not return to the zircon-type spectrum, the scheelite structure was retained. The electronic transition energies did not change dramatically since they were more sensitive to the local environment change and



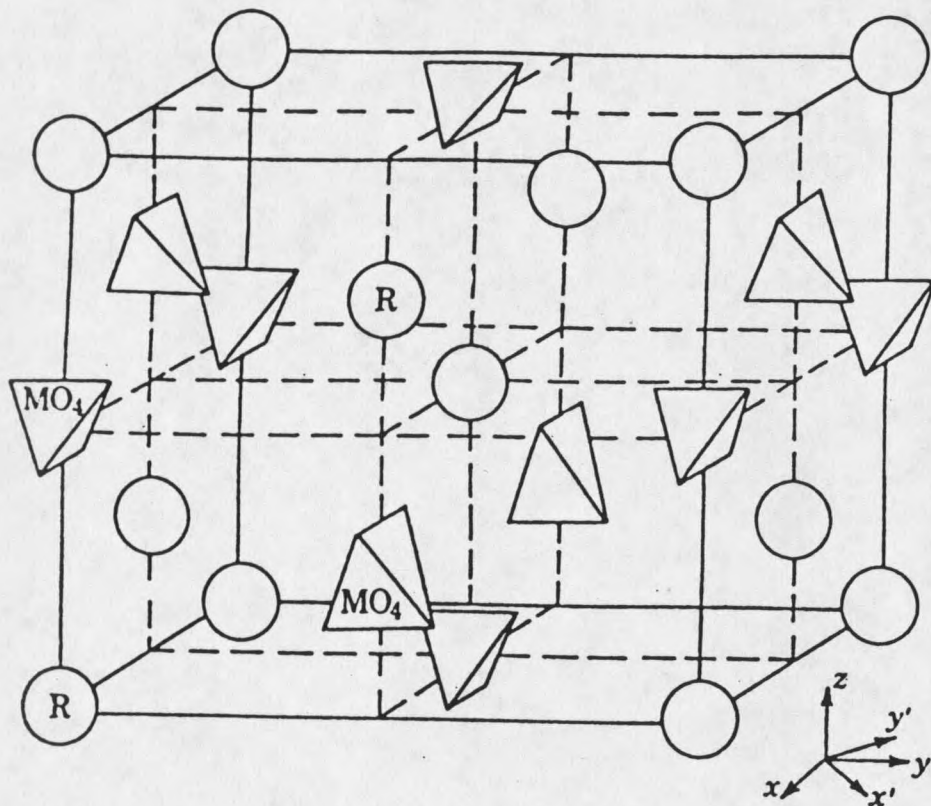
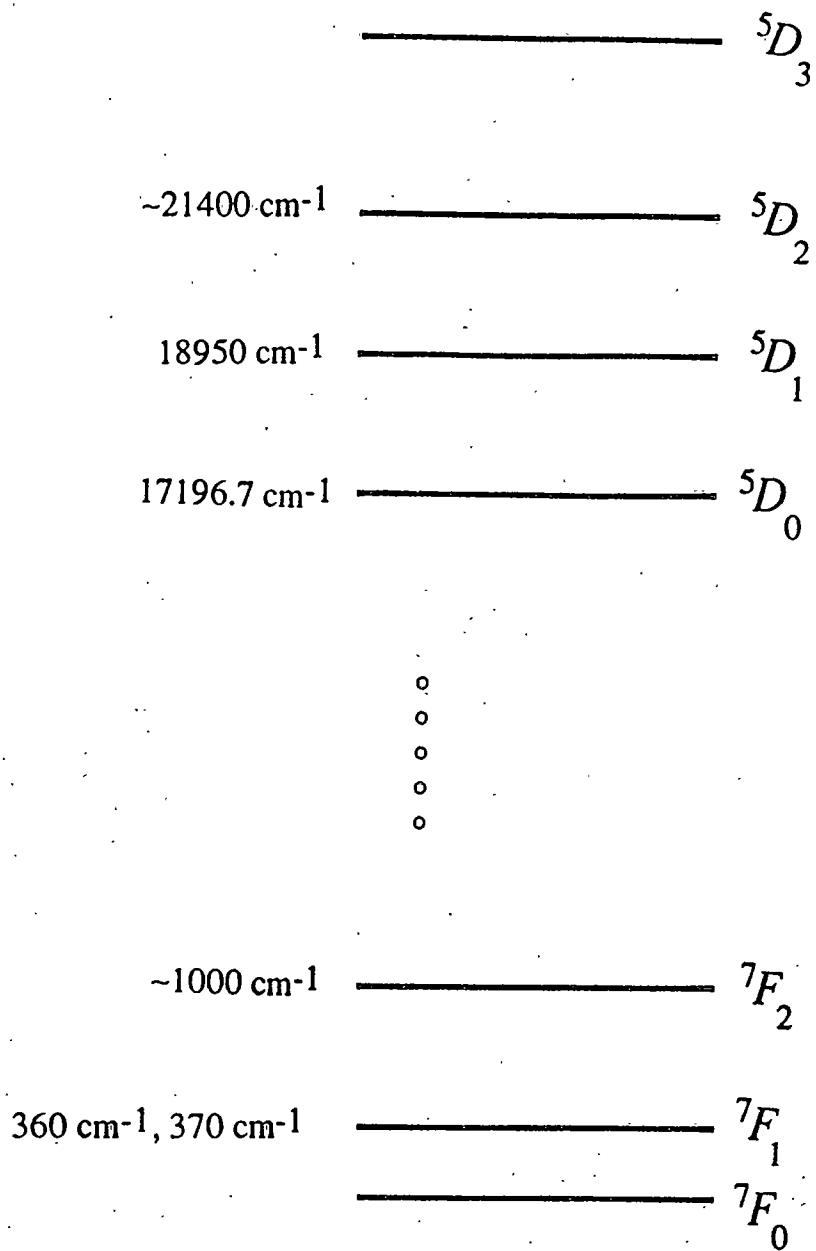


Figure 1.1 Schematic representation of the tetragonal zircon structure ( $D_{4h}^{19}$ ) for  $\text{RMO}_4$ . ( $\text{R} \equiv$  rare earth,  $\text{M} \equiv \text{V}, \text{As}, \text{or P}$ ). Two molecules per unit cell are indicated. (Wyckoff 1965, Elliott 1972)

relatively insensitive to the crystal structural change, but the  $\text{Eu}^{3+} \ ^5\text{D}_0$  lifetimes changed drastically in the two different phases (Chen *et al.* 1992).

The electronic structure of  $\text{Eu}^{3+}$  is simple compared to other trivalent rare earth ions. The ground state is always the  $^7\text{F}_0$  state (a possible scenario is that  $^7\text{F}_1$  was split so much by the crystal field that one of the three levels goes below  $^7\text{F}_0$ , but such a host has not been found yet). The  $^7\text{F}_1$  state is usually  $370 \text{ cm}^{-1}$  above the ground state. The  $^7\text{F}_2$  levels are around  $1000 \text{ cm}^{-1}$ . The  $^7\text{F}_J$  levels extend up to about  $5000 \text{ cm}^{-1}$ . From then on, a large gap of about  $12000 \text{ cm}^{-1}$  occurs until the next level  $^5\text{D}_0$  at  $\sim 17250 \text{ cm}^{-1}$ . The  $^5\text{D}_1$  levels are normally at  $\sim 19000 \text{ cm}^{-1}$ ,  $^5\text{D}_2$  at  $21400 \text{ cm}^{-1}$ , and  $^5\text{D}_3$  at  $24000 \text{ cm}^{-1}$ .  $^5\text{D}_4$ ,  $^5\text{L}_6$ , and even higher levels are more mixed up and difficult to determine from experiments. The levels that we are most concerned with in this work are summarized in Figure 1.2.

Brecher *et al* (1967, 1968) studied the spectrum of  $\text{Eu}^{3+}$  in  $\text{YVO}_4$  and  $\text{YPO}_4$ , and concluded that the crystal field parameter  $B_{20}$  had opposite signs for the two hosts. It was positive for  $\text{Eu}^{3+}:\text{YPO}_4$ , negative for  $\text{Eu}^{3+}:\text{YVO}_4$ . Other studies confirmed these observations. The lattice structures and the  $a/c$  ratios for these two hosts are not very different. The difference of  $B_{20}$  must come from the local oxygen coordinates. The crystal field seems to imply an oxygen octohedra elongated along the  $c$ -axis for  $\text{YPO}_4$  and an octahedra pressed along the  $c$ -axis for  $\text{YVO}_4$ , but this is not confirmed by structural studies. An interesting observation by Brecher *et al* (1968) was that the general crystal field fit was much better for  $\text{YPO}_4$  than for  $\text{YVO}_4$ . They attributed this phenomenon to the stronger covalency of the vanadates. We studied the polarized spectra of  $\text{Eu}^{3+}$  in  $\text{EuVO}_4$ ,  $\text{Eu}^{3+}:\text{YVO}_4$ ,  $\text{Eu}^{3+}:\text{LuVO}_4$ ,  $\text{Eu}^{3+}:\text{YPO}_4$ ,  $\text{Eu}^{3+}:\text{LuPO}_4$ , and  $\text{EuAsO}_4$ , and made crystal field calculations for each host. The general fit quality confirmed Brecher *et al*'s observation. These experiments and calculations will be presented in Chapter 2.



### $\text{Eu}^{3+}$ Energy Levels

Figure 1.2 Simplified energy level diagram of an  $\text{Eu}^{3+}$  ion.

Various vanadate, arsenate, and phosphate crystals undergo cooperative Jahn-Teller (CJTE) structural phase transitions at low temperature (Gehring and Gehring, 1975). Depending on the specific material, the phase transitions can either be structural or magnetic or both. Most of the structural transitions were driven by the coupling between degenerate or near degenerate ground state electronic levels and optical or acoustic phonons, or macroscopic lattice strain. Because of the transparency of these crystals, the CJTE effect in these compounds were suitable for optical studies and the transition mechanisms are particularly well understood compared to other Jahn-Teller systems (spinel, etc.).

Since  $\text{Eu}^{3+}$  has an isolated  $J = 0$  ground state with very little mixing with other levels, no phase transition is expected for europium compounds. But Zeeman experiments on the  ${}^5\text{D}_0 - {}^7\text{F}_1$  transition showed anomalously small Landé  $g$  factors for  $\text{EuVO}_4$ ,  $\text{Eu}^{3+}:\text{YVO}_4$ ,  $\text{Eu}^{3+}:\text{LuVO}_4$ , and  $\text{EuAsO}_4$ . Electronic Raman scattering on the stoichiometric compounds confirmed this observation. The apparent quenching of the angular momentum is attributed to the dynamic Jahn-Teller effect (Ham 1965). The fluorescence and Zeeman experiment will be presented in Chapter 2. The Raman scattering experiments and the dynamic Jahn-Teller effect will be discussed in Chapter 3.

In the fluorescence spectrum of  ${}^5\text{D}_0$  for  $\text{EuVO}_4$  and  $\text{EuAsO}_4$ , another anomaly appears as the double peak of the  ${}^5\text{D}_0$  to  ${}^7\text{F}_1$  singlet transition. Higher temperature absorption experiments confirmed the splitting of the  ${}^7\text{F}_1$  singlet level. The splitting of the singlet level in the stoichiometric compounds is proposed to be a Davydov splitting due to the exciton nature of the electronic states. The experiments leading to this conclusion will be presented in Chapter 2. The possible mechanism causing this splitting and other exciton phenomena will be discussed in Chapter 3 after the presentation of the dynamic Jahn-Teller interaction.

If a structural defect (impurity, vacancy, or interstitial) is present in a crystal, the active ions close to the defect will experience a different environment than in the ideal crystal. It can depart from the ideal environment by so much that numerous satellite spectral lines appear in the spectrum. Since there can be more than one active ion adjacent to the point defect and each one has a different environment, more than one defect site is present for each point defect. In a spectral region with many transitions, the different crystal fields associated with the various defect sites will give many transitions that overlap each other. The assignment of the spectral lines to the correct sites and transitions could be very difficult. The  $\text{Eu}^{3+}$  ion has the advantage that the ground state  ${}^7\text{F}_0$  and the excited state  ${}^5\text{D}_0$  are all isolated and are relatively insensitive to the crystal field, so that each spectral line in the  ${}^7\text{F}_0 - {}^5\text{D}_0$  region will correspond to a distinctive environment; a one-to-one relationship can be established between the spectral line and the crystal environment.

Cone *et al.* (1984) studied the excitation spectrum of stoichiometric  $\text{EuVO}_4$  in the  ${}^7\text{F}_0 - {}^5\text{D}_0$  region and found more than 50 defect lines scattered over  $50 \text{ cm}^{-1}$ , corresponding to over 50 distinct defect sites. Later experiments on a dozen different growths of  $\text{EuVO}_4$  found over 50 defect lines for each one of them (Robinson 1986, Cone *et al.* 1988, Lazzouni 1988, Hansen 1990, Cone *et al.* 1993). Stoichiometric  $\text{EuAsO}_4$  was also studied by laser excitation (Robinson 1986, Cone *et al.* 1988); a very "defective" spectrum was again found in the  ${}^7\text{F}_0 - {}^5\text{D}_0$  region. Excitation spectra for two additional growths of  $\text{EuVO}_4$  are given in Chapter 2. Because of the one-to-one relationship between the defect sites and the defect spectral lines, this kind of spectral map for the defect sites is very useful when other work is planned on the defect sites. We use the line labels from the spectra to label the defect sites. For example, when the property of line D is discussed, it is really the property of the site giving rise to the spectral line called line D.

Among all these defect lines, each has a distinctive fluorescence spectrum. In the  ${}^5D_0 - {}^7F_1$  spectra, generally more than three spectral lines (expected) are observed; energy transfer among the defect sites must be responsible for the extra fluorescence lines.

Chapter 4 addresses the energy transfer dynamics among these sites. Time-resolved fluorescence is used to find the donor-acceptor relations among them; and to determine the  ${}^7F_1$  levels of the donor. General systematics of the rare earth spectra in different hosts are considered in an attempt to interpret the  $\sim 50 \text{ cm}^{-1}$  shifts for the relatively crystal-field-insensitive  ${}^7F_0 - {}^5D_0$  transition. Energy transfer routes and lattice structures associated with defects will be discussed in the same chapter.

The europium nucleus has a spin of  $I = 5/2$  and possesses a strong quadrupole moment. In a crystalline environment, nuclear quadrupole splittings occur for different spin states. Splitting schemes are different for different crystal environments. Holeburning (Erickson, 1977a) was used to study the hyperfine splittings of these defect sites (Cone *et al.* 1984, Robinson 1986, Cone *et al.* 1988, Lazzouni 1988, Hansen 1990, Cone *et al.* 1992). Very different quadrupole splittings were found for the different defect sites. Nuclear Zeeman holeburning experiments were also used to study the defect sites in an effort to find the principal directions of the nuclear quadrupole interaction axes, and they were found to be strongly tilted (*ibid.*). A related technique - optically-detected nuclear-magnetic-resonance (ODNMR) - was used to study the ground state of these defects (Hansen 1990, Cone *et al.* 1992). Because of the strong and anisotropic quenching of the ground state  $\text{Eu}^{3+}$  nuclear magnetic moment (Elliott 1957, Cone *et al.* 1992), more parameters have to be used to fit the experimental data. Using only the Zeeman data for a magnetic field either along the  $a$ - or  $c$ -axis was not enough to make a successful fit of the data, so the full angular dependence of the spectrum was measured.

In this work, the ODNMR technique is extensively used to study the hyperfine structure of the defect ground states in  $\text{EuVO}_4$ . The nuclear quadrupole Hamiltonian and the hyperfine splitting measurements for over 30 defect sites at zero field will be presented in Chapter 5, with extensive discussions of the results and their implications. A new holeburning mechanism will also be discussed.

In Chapter 6, we present the angle-dependent ODNMR experiments on some of the defect sites in  $\text{EuVO}_4$ . These experiments were carried out with full angle rotation of the crystal in a magnetic field. Magnetic site inequivalence in a  $D_{4h}$  crystal will be discussed. Euler angles are used to define the defect coordinate system relative to the crystal. A fitting program taking into account the site inequivalence and the anisotropic nuclear magnetic moment was written for processing the angle-dependent experimental data. After a brief account of the apparatus, we will give the angle-dependent ODNMR results on some of the defect sites.

## CHAPTER 2

## PRIMARY SPECTROSCOPY AND CRYSTAL FIELD ANALYSES

In this chapter, we will present the absorption and fluorescence experiments on the stoichiometric  $\text{EuVO}_4$  and  $\text{EuAsO}_4$  crystals and on the europium doped  $\text{YVO}_4$ ,  $\text{LuVO}_4$ ,  $\text{YPO}_4$ , and  $\text{LuPO}_4$  crystals.  $\text{Eu(OH)}_3$  and  $\text{EuPO}_4$  were also studied for comparison. Defect line maps on the  ${}^7\text{F}_0 - {}^5\text{D}_0$  transition of two new  $\text{EuVO}_4$  crystals will also be presented.

Brecher *et al.* (1967, 1968) studied the polarized spectra of  $\text{Eu}^{3+}:\text{YVO}_4$  and  $\text{Eu}^{3+}:\text{YPO}_4$ . Those experiments were carried out at liquid nitrogen temperature without time resolution. Grenet *et al.* (1977) studied europium doped  $\text{GdVO}_4$ ,  $\text{YVO}_4$ , and  $\text{LuVO}_4$ , and made crystal field analyses for each situation. Their results will be discussed along with our analysis. We remeasured these spectra with time resolution, which has the advantage that at regions with many fluorescence peaks, the initial state can be distinguished by its lifetime signature. M. Bouzaoui (1991) carried out two-photon absorption experiments on the higher levels of  $\text{Eu}^{3+}:\text{LuPO}_4$ . Because of the different selection rules for one-photon and two-photon transitions, additional levels in the  ${}^5\text{D}_2$  region were determined in 2-photon experiments. We used those data in our analysis.

The energy levels of  $\text{EuVO}_4$  have been studied extensively by Cone *et al.* (1984), Lazzouni (1988), Hansen (1990), and Cone *et al.* (1993). Some of the results have been



used in this study. The  $\text{EuAsO}_4$  spectra have been studied by Robinson (1986) and Cone *et al.* (1988).

Zeeman experiments were used to measure the splittings of the energy levels. In particular, we focussed our attention on the  $^5\text{D}_0$ - $^7\text{F}_1$  transition. This transition, in the vanadates and  $\text{EuAsO}_4$ , has been found to have smaller Landé  $g$  factors than that expected for pure electronic states.

## Experiments

### Absorption Experiments

White light absorption experiments were employed to measure the  $^5\text{D}_2$  and  $^5\text{D}_1$  levels of  $\text{Eu}^{3+}$ . The experimental setup is shown in Figure 2.1, together with the fluorescence setup. A 55 W tungsten halogen lamp was used as the light source. A 75 mm lens focused an image of the lamp filament onto the crystal, which was immersed in pumped liquid helium. The crystal was normally masked by shim brass to minimize the stray light. The light exiting from the crystal was collected and collimated by a 75 mm  $f/2.8$  camera lens. The collimated light was then focused by a 200 mm  $f/3.5$  camera lens onto the slit of a SPEX 14018 scanning double monochromator (referred to as the SPEX in later discussions). Regular Polaroid polarizers were used just after the collecting lens to select the polarization measured. A quarter-wave plate was placed before the 200 mm lens to scramble the polarization in the monochromator.

The monochromator scanning was controlled by computer generated TTL pulses. Fifty pulses move the spectrometer *down* by one wavenumber. Since the SPEX has a maximum scan rate of  $130 \text{ cm}^{-1}/\text{s}$ , the pulses were generated at a much lower rate ( $\ll 6.5 \text{ KHz}$ ) so that they would not overwhelm the SPEX control box. The light signal was detected by an EMI9558QB photomultiplier at the exit slit of the spectrometer. The

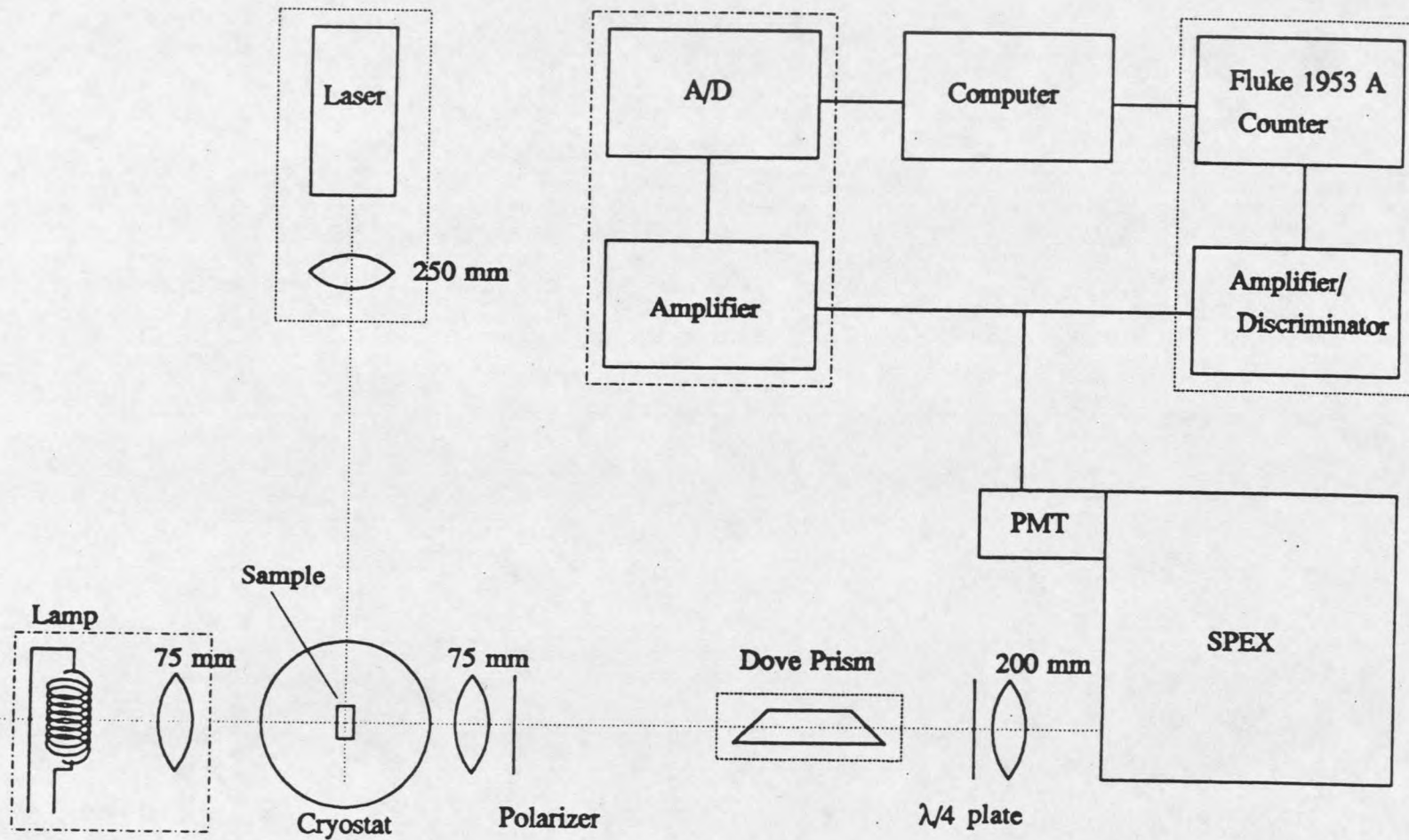


Figure 2.1 Experimental setup. Equipment blocked in dash-dotted lines was used only in absorption experiments. Those items blocked by dotted lines were used only in fluorescence experiments. Others are common to both.

output from the PMT was low-pass filtered and amplified by a Tektronix 7A22 amplifier, and then was fed to one channel of the DT2762 A/D converter. In the data acquisition process, the SPEX was set first and the light intensity was measured; then the spectrometer was scanned *down*, and the light intensity was measured again. An iron-neon hollow-cathode lamp was used to calibrate the SPEX.

The SPEX is most sensitive at around  $19000\text{ cm}^{-1}$ . We had the best signal in the  $^5D_1$  region, while that for the  $^5D_2$  levels was weaker.

### Fluorescence Experiments

In the fluorescence experiments, the laser was focused onto the samples by a 250 mm lens. When the laser frequency was tuned onto a transition peak, there would be fluorescence along the path of the laser beam. The fluorescence was collected at a  $90^\circ$  angle to the exciting beam direction. Otherwise, the collecting optics are identical to that used in the absorption experiments. A Dove prism was usually used between the 75 mm lens and the 200 mm lens to rotate the image of the fluorescence from the horizontal laser path to a vertical orientation so that most of the image can be focused onto the vertical monochromator entrance slit. This arrangement increased the signal by an order of magnitude in fluorescence experiments.

The output from the photomultiplier passed through a preamplifier and a discriminator before being converted to TTL pulses. These pulses were then sent to a GPIB-controlled Fluke 1953A counter/timer. Photon counting was the method of choice for fluorescence data. Monochromator scanning was the same as in the absorption experiment.

### Laser Excitation

Sometimes, measuring energy levels by absorption is simply impossible due to the weak transition probability. However, the immeasurable amount of absorption may result in observable fluorescence that can be detected easily because of the higher sensitivity of a fluorescence experiment. The dependence of the fluorescence intensity upon the excitation frequency can serve as a good indication as to where the transition occurs, and how wide and strong it is. The spectra measured by monitoring the fluorescence while scanning the laser excitation frequency are called excitation spectra. This way of measuring absorption does not always provide the same spectra as those measured by absorption experiments, but in case of extremely weak absorption, this may be the only alternative.

In our mapping of the defect  ${}^7F_0 - {}^5D_0$  spectra and in the measurement of the intrinsic  ${}^7F_0 - {}^5D_0$  transition in a magnetic field, laser excitation spectroscopy was used. A Coherent 599/21 single frequency cw dye laser was used to excite these transitions. The laser can scan 30 GHz ( $1 \text{ cm}^{-1}$ ) at one time. To map out a  $50 \text{ cm}^{-1}$  range, many "pages" of 30 GHz spectra had to be assembled together.

### Sample Temperature

Most of our experiments were carried out at pumped liquid helium temperature. This has the advantage that the phonon contributions to most of the transitions can be neglected. The results quoted in this thesis should all be at  $T < 2 \text{ K}$  unless otherwise indicated.

### Cryostats and Magnetic Fields

All our zero field experiments were carried out in a transverse access glass cryostat. In that dewar, the equipment layout was almost exactly like that shown in Figure 2.1.

The Zeeman experiments were carried out in a superconducting magnet dewar with an inner bore of about two inches. The magnetic field and supply current ratio was 1.00 kG/A. In this dewar, the layout changed a little in that the Dove prism was not used. Due to the axial access geometry, a mirror was used to send the light vertically into the dewar. The laser light was then reflected by a right angle prism to pass through the sample horizontally. A second prism sent the transmitted light out of the dewar for analysis in the absorption experiments. In fluorescence experiments, a third prism was used on the side to collect the fluorescence light for analysis. The fluorescence collection lens just outside of the dewar normally had a focal length of 330 mm.

#### Selection Rules

Group theory states that in order to have a dipole-allowed transition between an initial state represented by  $\Gamma_i$  and a final state represented by  $\Gamma_f$ , there must be an excitation mechanism represented by  $\Gamma_e$  so that  $\Gamma_i \times \Gamma_e$  contains  $\Gamma_f$ , where  $\Gamma_e$  is the representation either for an electric- or a magnetic-dipole (Tinkham 1964, for example).

From the multiplication tables given by Koster *et al.* (1963), selection rules in any symmetry may be determined. For  $D_{2d}$  symmetry, as laid out by Brecher *et al.* (1967), and restated by others (Macfarlane and Shelby 1987, Hansen 1990), the selection rules are listed in Table 2.1.

The compatibility table for this symmetry shows

$$J=0: \Gamma_1.$$

$$J=1: \Gamma_2, \Gamma_5.$$

$$J=2: \Gamma_1, \Gamma_3, \Gamma_4, \text{ and } \Gamma_5.$$

From the transition rules we can see that along the  $c$  axis, we see only the circularly polarized light originating from transitions with at least one doubly degenerate state as a terminal state, as would be expected since the  $a$  and  $a'$  axis should be equivalent.

Table 2.1. Selection rules in  $D_{2d}$  symmetry\*.

	$\Gamma_1$	$\Gamma_2$	$\Gamma_3$	$\Gamma_4$	$\Gamma_5$
$\Gamma_1$		M $\sigma$		E $\pi$	E $\sigma \alpha$ M $\pi \alpha$
$\Gamma_2$	M $\sigma$		E $\pi$		E $\sigma \alpha$ M $\pi \alpha$
$\Gamma_3$		E $\pi$		M $\sigma$	E $\sigma \alpha$ M $\pi \alpha$
$\Gamma_4$	E $\pi$		M $\sigma$		E $\sigma \alpha$ M $\pi \alpha$
$\Gamma_5$	E $\sigma \alpha$ M $\pi \alpha$	E $\sigma \alpha$ M $\pi \alpha$	E $\sigma \alpha$ M $\pi \alpha$	E $\sigma \alpha$ M $\pi \alpha$	E $\pi$ M $\sigma$

\* In  $\text{Eu}^{3+}$ , all transitions for which  $\Delta J \neq \pm 1$  obey electric-dipole selection rules. For  $\Delta J = \pm 1$ , magnetic-dipole rules are obeyed when  $J = 0$  is one of the terminal states. Otherwise, the transition will be of mixed character.

E denotes electric-dipole; M, magnetic-dipole;  $\pi$ , electric vector parallel to  $c$ -axis;  $\sigma$ , electric vector perpendicular to the  $c$ -axis;  $\alpha$ , circularly polarized around the  $c$ -axis.

### Crystals

We have studied a range of europium-doped zircon-structured crystals of different  $\text{Eu}^{3+}$  concentrations. The stoichiometric  $\text{EuVO}_4$  crystal we used most was grown in the Clarendon Laboratory of the University of Oxford by B. Wanklyn. It was colorless and about  $1 \times 1.5 \times 3 \text{ mm}^3$  in size and was classified as growth A in Cone *et al.* (1993) and Hansen (1990). An  $\text{EuVO}_4$  crystal classified as growth I by Cone *et al.* (1993) was studied using angle-dependent optically-detected nuclear-magnetic-resonance (see Chapter 4). Another growth of  $\text{EuVO}_4$  crystals obtained from the University of Oxford were doped with 1% praseodymium; it also had a tint of brown color. Other  $\text{EuVO}_4$  samples used were grown by Dr. M.M. Abraham of Oak Ridge National Laboratory on 22 Nov 1991; these crystals have a brownish color and are transparent. They have not







































































































































































































































































































































































































































